Derivation and Validation of High-Resolution Digital Terrain Models from Mars Express HRSC Data

Klaus Gwinner, Frank Scholten, Michael Spiegel, Ralph Schmidt, Bernd Giese, Jürgen Oberst, Christian Heipke, Ralf Jaumann, and Gerhard Neukum

Abstract

The High Resolution Stereo Camera (HRSC) onboard the Mars Express mission is the first photogrammetric stereo sensor system employed for planetary remote sensing. The derivation of high-quality digital terrain models is subject to a variety of parameters, some of which show a significant variability between and also within individual datasets. Therefore, adaptive processing techniques and the use of efficient quality parameters for controlling automated processing are considered to be key requirements for DTM generation. We present the general procedure for the derivation of HRSC high-resolution DTM, representing the core element of the systematic derivation of high-level data products by the Mars Express HRSC experiment team. We also analyze test series applying specific processing variations, including a new method for signal adaptive image preprocessing. The results are assessed based on internal quality measures and compared to external terrain data. Sub-pixel scale 3D point accuracy of better than 10 m and a DTM spatial resolution of up to 50 m can be achieved for large parts of the surface of Mars within a reasonable effort. This confirms the potentials of the applied along-track multiple stereo imaging principle and allows for a considerable improvement in our knowledge of the topography of Mars.

Introduction

The High Resolution Stereo Camera (HRSC: Neukum *et al.*, 2004; Jaumann *et al.*, 2007) onboard the European Space Agency (ESA) mission Mars Express (MEX) is the first photogrammetric stereo sensor system employed in planetary remote sensing. In contrast to the stereo mapping instruments of other planetary missions with dedicated photogrammetric capabilities, such as Viking, Clementine, Mars Global Surveyor, and Mars Reconnaissance Orbiter (Snyder, 1979; Nozette *et al.*, 1994; Malin an Edgett, 2001; McEwen *et al.*, 2007), HRSC has the unique capability of simultaneous acquisition of stereo imagery. This avoids changes of imaging conditions which may occur between different orbital passes and makes pointing maneuvers for obtaining stereo coverage unnecessary. HRSC, operated in Mars orbit since January 2004, is a multi-line pushbroom stereo camera providing up to five panchromatic multi-angle observations of the surface during each orbit (Figure 1). Simultaneously, multi-spectral imagery is acquired by four CCD lines equipped with spectral filters (near-infrared, red, green, blue). A nominal ground resolution of up to almost 10 m/pixel is being achieved. Surface reconstruction from HRSC data can be based on the multi-stereo principle, which allows for improved reliability, quality control, and automation by enhanced visibility conditions and by over-determined intersections. In addition, stereo processing benefits from nearly time-synchronous acquisition of the stereo observations. These capabilities of multi-line stereo sensors have been implemented and tested in a number of Earth-oriented airborne and spaceborne applications using different sensor systems (Hofmann *et al.*, 1982; Müller, 1991; Ebner *et al.*, 1996; Wewel *et al.*, 2000; Gwinner *et al.*, 2000; Sandau *et al.*, 2000; Grün and Zhang, 2003; Scholten and Gwinner, 2004).

HRSC aims at global coverage of planet Mars with high-resolution DTM (up to 50 m horizontal resolution) and is thus complementary to the meter-scale elevation models (10 m horizontal resolution and better) which have been or will be produced from Mars Orbiter Camera narrow-angle images (MOC-NA: Kirk *et al.*, 2003) and Mars Reconnaissance Orbiter High Resolution Imaging Science Experiment data (MRO-HIRISE: McEwen *et al.*, 2007, Kirk *et al.* 2007), since these will be available only on the very local scale. From Viking data, global topographic mapping of Mars at 1: 2 000 000 scale with 1-km contours has been achieved (Wu and Doyle, 1990). More recently, global topographic coverage with a spatial resolution of about 300 m × 1000 m at the equator, and better near the poles, has been achieved

Klaus Gwinner, Frank Scholten, Bernd Giese, Jürgen Oberst, and Ralf Jaumann are with the Institute of Planetary Research, German Aerospace Center (DLR), D-12489 Berlin, Germany Rutherfordstr. 2 (Klaus.Gwinner@dlr.de).

Michael Spiegel is with Photogrammetry and Remote Sensing, Technische Universität München, D-80333 München, Germany.

Ralph Schmidt and Christian Heipke are with the Institute of Photogrammetry and GeoInformation, Universität Hannover, D-30167 Hannover, Germany.

Gerhard Neukum is with the Remote Sensing of the Earth and Planets, Freie Universität Berlin, D-12249 Berlin, Germany.

Photogrammetric Engineering & Remote Sensing
Vol. 75, No. 9, September 2009, pp. 1127–1142.

0099-1112/09/7509–1127/$3.00/0

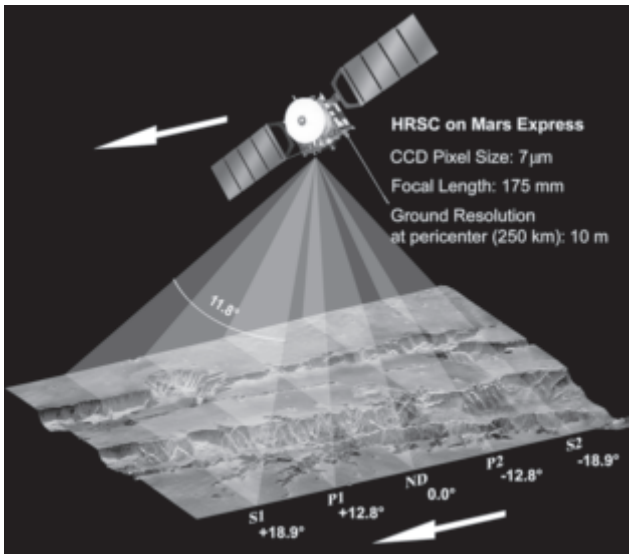

Figure 1. Stereo imaging principle of HRSC, a multi-line pushbroom stereo camera.

by the Mars Orbiter Laser Altimeter (MOLA) instrument on Mars Global Surveyor (Smith *et al.*, 2001).

Based on airborne experiments applying the HRSC qualification model, experience on the potential of HRSC stereo imagery for surface reconstruction has been gained prior to the launch of Mars Express. These experiments were based on an earlier (and modified) version of the HRSC processing system developed for planetary remote sensing (in the next section) and have included the stereo mapping of areas with high relief, as well as the stereo mapping of surface types and morphologies similar to planetary terrain (Gwinner *et al.*, 1999 and 2000; Wewel *et al.*, 2000). However, the derivation of digital terrain models (DTMs) from Mars Express HRSC stereo imagery in addition is complicated by a number of conditions related to the atmosphere and surface of Mars, as well as to the characteristics of the imaging system. In particular, data acquisition from Mars orbit includes specific constraints that cause a reduction of the radiometric (8-bit nominal) and geometric resolution of the image data. A common problem, for example, is the contrast reduction resulting from a local or temporal increase of the atmospheric optical depth associated with dust and hazes, as frequently met at high-northern and mid-southern latitudes, as well as near terminator crossings. High optical depths cause an additional background signal from the atmosphere and a reduction of the energy reflected from the surface towards the sensor due to scattering and absorption. The contrast loss is not predictable and may lead to significant reductions in the local dynamic range. It also has a direct impact on the compression ratio of the imagery.

Compression of HRSC imagery is based on a hardware implemented JPEG variant of the direct cosine transform (Schwarz, 1995) and is, therefore, not lossless. The compression factor cannot be selected directly but is controlled by a quality factor. Compression rates typically amount to factors of 4 to 40 and show across-track as well as along-track variations depending on the texture properties of the scene. This selectivity of compression is, under the constraint of strictly limited data rates, a feature that aims at capturing areas displaying rich surface texture with maximum resolution (low compression). Conversely, low-texture areas show stronger compression. Contrast reduction associated with high optical depths therefore tends to increase the compression rate locally. The quality reducing factors introduced by the compression are image block artifacts (through separate compression of non-overlapping 8×8 image windows) and manipulation of the spectral domain by encoding of transform parameters with reduced accuracy. These modifications to image texture and the local greyvalue distribution introduce artificial dissimilarity to the stereo images which affects the quality of image matching (described in the *Processing Approach for High-resolution DTM* subsection). While it has been demonstrated that subpixel precision matching is feasible under certain circumstances in spite of JPEG compression (Parkes *et al.*, 1991), it is also known from experiments using aerial photography that image compression may significantly degrade the overall results of automated DTM generation (Robinson *et al.*, 1995). HRSC image examples demonstrating the effects of compression are presented in Figures 3a and 3b.

Further variability is introduced by the quality of the available orbit and pointing data, which is not constant. Due to the orbit characteristics of Mars Express, also illumination conditions and ground resolution vary within a considerable range. The geometric resolution of the imagery (up to ~10 m/pixel) depends on the height of the elliptical orbit at the time of data acquisition and on the current macro-pixel format setting for the respective channel. Macro-pixel formation is a specific feature of the camera and allows for on-board integration of CCD-pixels in along-track and across-track direction for reducing data rates at the cost of spatial resolution. In addition, the effective geometric resolution depends on the actual compression rate.

In the Photogrammetric Processing Section, we present the general procedure for the derivation of HRSC high-resolution DTM, representing the core element of the systematic derivation of high-level data products for Mars by the Mars Express HRSC experiment team. A test series applying different processing variations was performed (in the Experimental Setup Section), with the goals of testing improved procedures for data processing, and of a detailed assessment of the capabilities HRSC offers for the generation of high-resolution DTMs for Mars. We focus on the internal accuracy of the DTM, which primarily depends on the precision and density (i.e., number per area) of the derived 3D points. The major practical aspects of internal accuracy are the completeness of the surface description, the level of detail, and morphologic consistency. While aspects of absolute accuracy with respect to a geodetic reference system have been considered elsewhere (Spiegel *et al.*, 2005; Spiegel, 2007), a further focus of the present work is on the effect of bundle adjustment on the generation of high-resolution DTMs. Quality assessment for the results of surface reconstruction is based, firstly, on statistical properties of intermediate processing results relevant to the precision of height and position and, finally, to the DTM resolution that can be achieved (in the Results section). The results are compared to existing topographic data from the MOLA experiment (NASA, 2003). The discussion of the results also considers implications for the systematic derivation of HRSC high-resolution DTMs (in the Summary and Conclusions Section).

Photogrammetric Processing

HRSC Data Processing System

For HRSC data processing, a comprehensive software system based on the VICAR planetary image processing system has been developed (JPL, 2003; Scholten *et al.*, 2005). The

system includes modules for the systematic preprocessing and calibration of the raw data as well as modules for photogrammetric processing. Among the latter, modules for image rectification, map projection, image matching, 3D point calculation, and raster interpolation are used for DTM generation. A similar system is applied for the derivation of high-resolution photogrammetric products from airborne digital stereo data for a number of years (Wewel *et al.*, 2000; Scholten and Gwinner, 2004). The modifications and developments for the specific task of deriving Mars Express HRSC high-resolution DTMs are presented in this paper.

Photogrammetric analysis of HRSC data uses radiometrically-calibrated imagery. The stereo images are amended by orbit and pointing data and instrument geometric calibration data. These base data are available using the Planetary Science Archive (PSA) and Planetary Data System (PDS) catalogues (**http://www.rssd.esa.int/PSA**; **http://pds.jpl.nasa.gov**). Fully automated data processing is routinely applied for the HRSC stereo images of all mapping orbits immediately after data receipt in order to provide preliminary orthoimages and DTMs with 200 m grid spacing (Scholten *et al.*, 2005). The first priority for these early data products is fast availability. No quality control is applied, and orientation data is not improved by bundle adjustment and is not necessarily based on the final version of the navigation data derived by ESA. The preliminary 200 m DTM is used for initial scientific assessment of new data, while detailed studies generally require more evolved 3D data products.

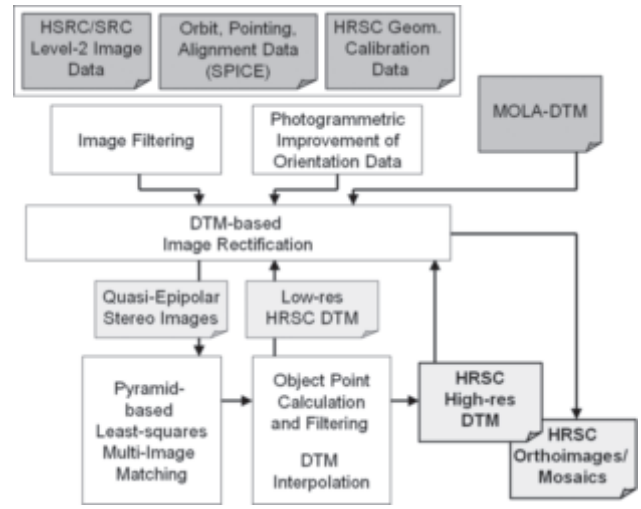

Figure 2. Overview of the proposed processing system for the derivation of high-resolution DTM, and its integration into the overall procedure for systematic derivation of Mars Express HRSC high-level data products.

Processing Approach for High-resolution DTM

The setup of the procedures for deriving high-resolution DTMs differs from the production of the preliminary 200 m DTM by the application of additional procedures, a revised approach to parameter selection, and the inclusion of standardized procedures for quality control. While the algorithm for image matching is certainly the most central part of the processing chain, further critical steps consist in an appropriate preprocessing of the image data, blunder detection and DTM interpolation, and the improvement of the exterior orientation data. Due to the variability of the input data, the application of adaptive processing techniques is considered to be a key element for the derivation of HRSC high-resolution DTMs with standardized quality characteristics.

Figure 2 presents an overview of the proposed processing approach for deriving high-resolution DTMs, and shows its integration into the overall procedure for systematic derivation of Mars Express HRSC high-level data products. Note that different techniques for further analysis of HRSC 3D data, not shown here, have been proposed (Albertz *et al.*, 2005; Kirk *et al.*, 2006; Heipke *et al.*, 2007), of which some can be combined with the presented approach. DTM results obtained by using this approach have also been systematically inter-compared with results obtained by applying other software systems. The test was organized by the Photogrammetry and Cartography Working Group within the HRSC Co-Investigator Team under the auspices of the ISPRS Working Group IV/7 on Extraterrestrial Mapping (Heipke *et al.*, 2007).

Image Preprocessing

Preprocessing of HRSC stereo images is considered an essential step for DTM generation since compression features may lead to erroneous point correlation. A large number of algorithms have been proposed for the task of enhancing JPEG-compressed images (see Nosratinia *et al.*, 2001). With regard to the large data volumes of remote sensing imagery, the time efficiency of the algorithms is a relevant issue. While some of the techniques include computationally rather intensive algorithms (e.g., image restoration using regularization techniques or stochastic modeling based on Markov Random Fields (Yang *et al.*, 1993; O'Rourke and Stevenson, 1995), the least computing cost is required for space-invariant filtering techniques which have been used in the earliest attempts for enhancing block-encoded images (Reeves and Lim, 1984). Space-invariant filtering is, however, known to be not very efficient for this application since it may either tend to smooth the image too strongly or not suppress artifacts sufficiently. In order to allow greater flexibility to the filtering process, space-variant filters have been investigated (e.g., Kuo and Hsieh, 1995). A main task in the design of a space-variant filter for a specific application is to identify a specific local image characteristic that can be used for controlling the intended variations of the filter characteristics. This characteristic may differ for different image data sources.

We developed an adaptive Gaussian low pass filtering algorithm with variable bandwidth for HRSC image preprocessing. Since its low pass characteristic is made dependent on local image statistics, the filter allows us to take local variations of the effective spatial resolution into account. While it reduces high-frequency noise components, low pass filtering also improves the radiometric accuracy of the filtered image data and may thus enhance the sub-pixel accuracy of the correlation. The filtering kernel is given by a normalized and centered two-dimensional Gauss function within the ranges of $\pm 2\sigma$ for both independent variables. The criterion for space-variant scaling of the filter dimension is a threshold value E_T of the local information content $E = -\Sigma_j\, p_v\, ld\, p_v$ (in bit), where p_v is the relative frequency of gray value v in a test window of size j, i.e., the fraction of pixels with gray value v within the test window; *ld* is the dyadic logarithm. During the filtering process, the window size is reduced stepwise (by two pixels) and independently for each pixel position until a value of the local information content smaller than E_T is obtained. E attains low values in image areas associated with large compression ratios. Figure 3a-I shows a compressed image example of particular interest, because an HRSC image sequence acquired only few days earlier and without data compression is available (Fig 3a-III). Figure 3a-II shows the

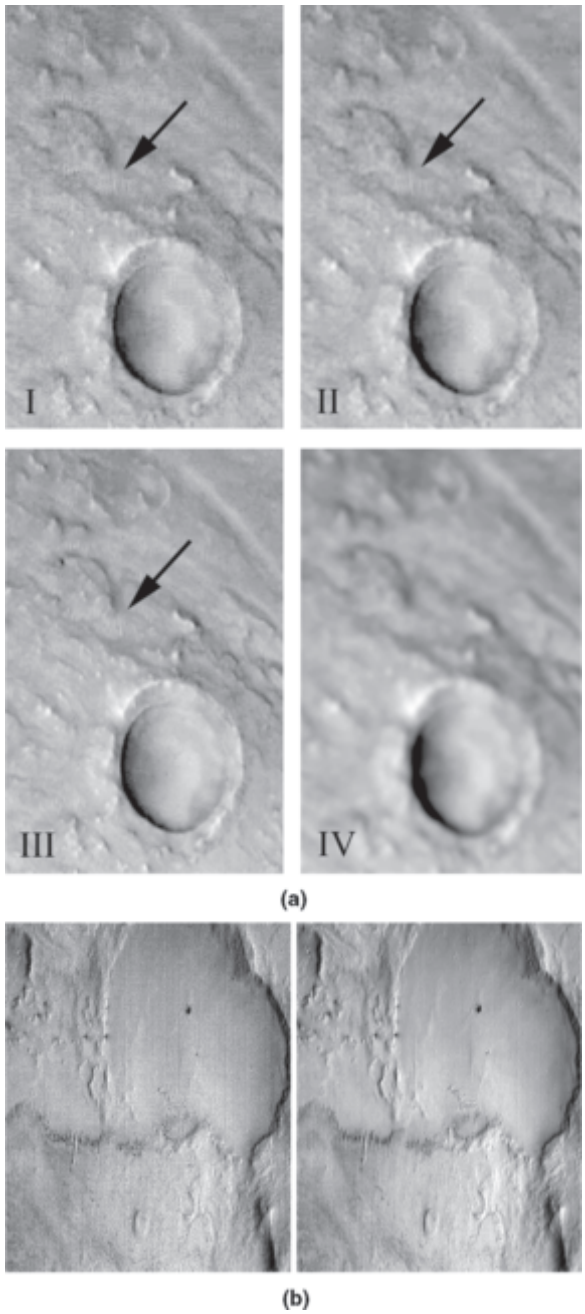

Figure 3. (a) Detail of HRSC stereo-1 channel image from orbit MEX 3047, showing compression patterns (image I) and different filtering results. Image III is from a HRSC image sequence of the same area which has been acquired without data compression (MEX orbit 3036). Edges and small image details such as dune structures (arrows) are preserved in the adaptive filtering result (image II), while compression patterns are suppressed. Image IV has been derived by space-invariant filtering which causes loss of high-frequency patterns. Width of image subsets is 150 pixels in the original image (corresponding ground distance about 5 km); and (b) Left: Original image of stereo-2 channel, MEX Orbit 0335, Right: after filtering with adaptive Gaussian low pass filter. Size of image subset is 1980 × 1680 pixels.

adaptive filtering result for image 3a-I using an initial window size of nine pixels (typical initial window sizes for panchromatic HRSC images are in the range seven to eleven pixels). Comparison with image 3a-III demonstrates the resulting suppression of blocky compression structures (best visible on smooth surfaces), while edges are preserved and small surface features in well-textured areas such as the light-colored dunes present in some places (see arrow) are still discernible. The initial window size can be set to a value that matches the size of the largest compression artifacts without affecting this behavior. In contrast, applying a Gaussian low-pass filter with a fixed size that is large enough for effective reduction of all compression patterns leads to a significant loss of fine surface textures and to degraded edges (Fig 3a-IV, filter size seven pixels). Figure 3b shows a further adaptive filtering result for a larger image sub-area.

Image Matching

Area-based image matching based on cross correlation and least-squares sub-pixel adjustment (Ackermann, 1984) is applied for determining conjugate points in multiple stereo channels automatically (multi-image matching). A common scale is used for the different stereo channels, regardless of initial scale differences between the images. The matching procedure is applied to quasi-epipolar images produced by differential rectification. We use the term quasi-epipolar geometry here to denote rectified stereo images of a push-broom camera which display near-zero parallaxes parallel to scan lines (y-parallaxes). This property increases the efficiency of image matching significantly because it allows us to introduce an indirect epipolar constraint by reducing search areas to the actually expected residual parallaxes. In general, the validity of this epipolar assumption depends on the precision of the sensor attitude data, which is usually about the scale of one pixel for Mars Express and thus sufficiently high, and on the straightness of the platform motion (generally very smooth for orbital data).

The procedure for generating the quasi-epipolar images used for matching is implemented as a two-stage process. First, a low-resolution HRSC DTM is obtained from quasi-epipolar images derived by ortho-rectification using a MOLA DTM. In the second stage, the low-resolution HRSC DTM is used for ortho-rectification to obtain improved quasi-epipolar images for the final matching. The introduction of a low-resolution HRSC DTM is aimed primarily at a higher efficiency and completeness of image matching in high-relief terrain, where representation of detailed topography in the MOLA DTM can be insufficient for our purposes. Note that the matching criteria applied are not constrained by any *a priori* height information. Thus, the introduction of neither the MOLA DTM nor the low-resolution HRSC DTM contributes directly to the heights to be derived from the matched HRSC points. The spatial resolution of the low-resolution HRSC DTM depends on the actual best ground sampling distance and typically ranges between 500 m and 1,000 m.

In addition to the overall two-stage design, the matching process is refined stepwise using image pyramids. Conjugate points are searched according to a regular search grid defined in a master image selected among the multiple stereo images (usually the nadir channel image). Approximate conjugate point coordinates are determined in reduced images that correspond to a specific pyramid level by cross correlation of sub-images, and are refined subsequently using the next pyramid level. Finally, approximate point coordinates are refined with sub-pixel accuracy in the full-resolution image by least-squares adjustment. Both the cross correlation coefficient and the quality of sub-pixel adjustment are used to reject unsafe point correlations. In

addition, textural properties of the sub-images are checked within the correlation procedure and can lead to the rejection of unsafe correlations. Multiple images are matched with the master image one by one, the resulting point pairs are combined at the stage of object point calculation. Due to the projective distortions of the master image (and, if applicable, due to differing map projections), the search grid used for matching is not congruent with the final DTM grid.

Bundle Adjustment and Co-registration to MOLA

Improvement of exterior orientation data for HRSC data processing is achieved by bundle adjustment that uses geometric control information derived from MOLA data as an additional input (Ebner *et al.*, 2004; Spiegel *et al.*, 2005; Spiegel, 2007). A similar approach has been applied to MOC stereo data by Yoon and Shan (2005). The three-dimensional position of the spacecraft is constantly determined by ESA applying a combination of doppler shift measurements, ranging data, triangulation measurements, and orbit analysis. The nominal orbit accuracy at the pericenter shows considerable variations for the mission (10 to 2,120 m along track, 3–795 m across track, 1 to 80 m radial height (Hechler and Yanez, 2000). The attitude of the spacecraft is derived from measurements of star tracker cameras and from an Inertial Measurement Unit (IMU). The pointing accuracy results from a combination of attitude errors and navigation errors with a nominal value of 25 mdeg for pitch, roll, and yaw (Astrium, 2001). All external geometric information is provided in the SPICE kernel format (**http://naif.jpl.nasa.gov**) used in most planetary missions.

The bundle adjustment process uses tie point datasets automatically generated by image matching as input data (Heipke *et al.*, 2004; Schmidt *et al.*, 2005). The adjustment procedure consists of two main steps (Spiegel *et al.*, 2005). In the first step, a bundle adjustment without control information is performed in order to improve the pitch and yaw angles along the entire orbit and to identify possible matching problems by a robust adjustment. The mathematical model of the bundle adjustment is based on the collinearity equations which are linearized by a truncated Taylor expansion. In the second step, HRSC object points are registered to the existing geodetic reference system of Mars which requires additional control information. Since classical ground control points are not available in sufficient quantity for Mars, control surfaces derived from the MOLA DTM (NASA, 2003) are used, which results in improvements for all six parameters of the exterior orientation.

On the basis of the final high-resolution DTM, the co-registration with the MOLA DTM is checked using average height differences for sub-sets of the DTMs. These checks usually reveal residual horizontal offsets smaller than the grid spacing of the HRSC DTM and residual vertical offsets below 10 m, i.e., on the order of the point accuracy of the MOLA control information used by the bundle adjustment (Neumann *et al.*, 2003). Due to their regional-scale nature, these residual offsets can be determined and corrected based on trend surface analysis applied to height difference maps (i.e., from a number of data points significantly larger than the number of tie points used for bundle adjustment).

Object Point Calculation and DTM Interpolation

The conjugate point coordinates obtained by image matching are back-transformed to the original image coordinates using stored transformation parameters, and then combined with interior and exterior orientation data for forward ray intersection. Least-squares adjustment is applied for this overdetermined problem. The result is a file of 3D points (object points) together with their relative accuracy defined in body-fixed Martian Cartesian coordinates.

For the generation of a raster DTM (16-bit integer data format; numerical height resolution 1 m), object points are transformed to a geographic latitude/longitude/height reference system, i.e., the Mars sphere as defined by the MOLA science team (Smith *et al.*, 2001), and are combined on a pixel basis by Gaussian distance weighted averaging within a local interpolation radius. Gap areas with insufficient point coverage are filled using a raster pyramid, where each raster level is derived by scale reduction of the previous one by a factor of 2, and the height value of a gap pixel is obtained from the first raster level for which the required point number is achieved.

For the choice of the DTM grid size, a value of about twice the spacing of the search grid used for matching (rounded to multiples of 25 m) has proven feasible. This definition of the DTM grid size has been adopted as a compromise between the smallest horizontal spacing of the 3D points (i.e., the smallest sampling distance according to signal theory terminology) and the need to allow for some variation in the quality and distribution of the object points, considering the fact that their precision and lateral spacing are not ideally constant over the DTM area. The best choice of the matching resolution is generally dominated by the mean stereo image resolution. However, specific camera operation modes as well as the actual textural image properties can also be important. In practice, the simultaneous use of different matching resolutions is found profitable, and multiple matching tests based on image resolutions corresponding to the ground resolution reduced by factors of 2 to 5 are routinely performed. Object points derived from multiple matching runs at different resolutions are combined by distance weighted averaging during DTM interpolation.

In order to eliminate outliers, object points associated with an intersection error larger than a chosen level of the error distribution are excluded from DTM interpolation. The intersection error of an individual object point provides a measure for its relative 3D accuracy. The error is derived from the improvements of the orientation data that result from achieving an optimal intersection of the conjugate rays in terms of least-squares adjustment. The improvements are converted into error components *dx*, *dy*, *dz* of the body-fixed Cartesian point coordinates. Note that the 3D intersection error thus defined provides an upper limit for any of the error components in an arbitrary Cartesian coordinate system, e.g., for the height error in a local tangential system. As a second selection criterion for object points, a minimum required number of simultaneous stereo observations can be defined.

Parameter Selection

As a consequence of the variable properties of the input data, no unique set of fixed processing parameters can be considered as optimal for high-resolution DTM processing of HRSC data. Since the number of relevant parameters is very large, parameter rules for adaptive parameter setting are applied. Their implementation includes case sensitive selections among pre-defined alternative parameter subsets as well as functional definitions based on characteristics of the input data and of intermediate results. For this reason, some of the quality measures applied in the analysis of the test series presented in the Results Section are of high practical significance for DTM processing since they are used to control the parameter setting.

Parameter rules allow us to adjust the processing parameters fully automatically based on a limited set of initial values. In practice, however, individual quality checks should generally be included in order to achieve best possible DTM results, since they may lead to specific modifications of the parameter setting for the particular

TABLE 1. COMMON PARAMETER SETTING USED IN THE TEST RUNS (SELECTION OF THE MORE RELEVANT PROCESSING PARAMETERS)

Parameter	Parameter Value	Explanation
Matching Image Geometry	quasi-epipolar, common scale	Geometric properties of the multiple images used for matching
Height Data for Rectification (quasi-epipolar images)	low-res HRSC DTM	DTM providing height information for differential rectification to generate images used for matching; MOLA 463m-DTM for deriving the low-res HRSC DTM
Matching Resolution	4× nominal nadir resolution	Spatial resolution of the quasi-epipolar images used for matching, in m/pixel
Dim. Cross Correlation Window	13–15 pixels	Side length of image window used for cross correlation, depending on image resolution
Dim. Least Squares Correlation Window	15–19 pixels	Side length of image window used for least squares correlation, depending on image resolution
Initial Cross Correlation Threshold	0.4	Min. required initial cross correlation coefficient for starting least squares matching
Final Cross Correlation Threshold	>0.6	Min. required cross correlation coefficient for accepting a matching result
Max. Intersection Error	95 % level of the error distribution	Threshold for rejection of object points
Min Number of Intersections	3	Min. required number of stereo observations to accept an object point
DTM Interpolation Method	Distance Weighted Mean	Interpolation method for deriving a DTM grid value from object points within a local interpolation radius
Object Point Symmetry	0.2	Max. allowed horizontal deviation between the center of gravity of all object points within interpolation radius and the center of the grid cell, as a fraction of cell size

case. In order to facilitate the comparability of the results, such manual fine-tuning of parameters has not been applied in the test series described below. Instead, a common set of parameter definitions has been used here, including a common set of parameter rules for the automatic adjustment of parameters. The parameter definitions for the test runs are described in the following section and in Table 1).

Experimental Setup

Based on the procedures described above, an experimental test series comprising six different processing variations and 30 orbits of the first year of the mission (approximately 40 GB of raw data) has been set up to assess the potential of HRSC for the generation of high-resolution DTMs. The test data cover about 2 million km^2 of the Mars surface, i.e., some few percent of the total coverage achieved during the nominal mission (two Earth years). The total number of object points derived during the test runs is larger than 1.2 billion. The respective areas range in latitude between 50°N and 40°S and cover a variety of different terrain types (e.g., graben systems, plains, Southern Highland terrain, shield volcanoes, fluvial erosion features). The dataset also covers the full range of nominal resolutions from maximum (of about 10 m/pixel, nadir channel) to lower resolution orbits (>50 m/pixel, nadir channel). With regard to possible dependencies on spatial resolution, a relatively large number of low-resolution orbits (as compared to the entire HRSC dataset) have been included (Figure 4). In addition to a wide range of image resolutions and the coverage of different terrain types, no specific selection criteria have been applied. With few exceptions, the datasets include five panchromatic stereo images with macro pixel binning 1 × 1 (nadir channel), 2 × 2 (outer stereo channels), and 4 × 4 (remaining two stereo channels). The number of image lines ranges between 25,000 and 141,000 for the nadir lines, corresponding to the full size of the image sequence acquired on the respective orbit.

For all test datasets, three preprocessing variations were generated. They comprise, first, stereo imagery without filtering, second, space-invariant low pass filtering (Gaussian low pass with σ = 1.8 pixel), and, third, adaptive filtering based on the method presented in the Image preprocessing section. For all variations, one complete DTM run was based on nominal orientation data (drift-corrected timeline data, reconstructed orbit data and nominal pointing data), and a second one on exterior orientation data improved by bundle adjustment, thus increasing the total number of tested variations to six.

Bundle-adjusted orientation data were available for 23 of the 30 datasets. In the remaining seven cases, bundle adjustment was aborted due to failure to correlate MOLA pass information (on smooth terrain) or due to unreliably small relative improvements for low-resolution images. This success rate for the test orbits is consistent with the overall success rate of bundle adjustment achieved for all

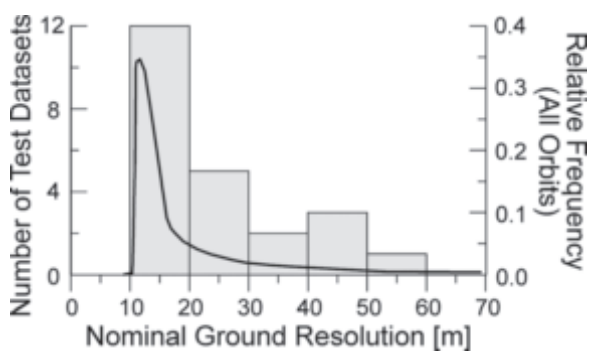

Figure 4. Histograms of nominal ground resolution (nadir channel) for the test dataset (bar chart) and of all datasets up to MEX orbit 2195.

datasets, while the number of successfully adjusted orbits and the range of image resolutions in the test are still representative.

Apart from the parameters of image preprocessing, the same set of parameter definitions (including identical parameter rules) was applied for each variation and each dataset (see listing of parameters in Table 1). Thus, in the case of the test runs, no parameters have been adjusted manually in order to achieve a particularized suitability for individual orbits.

Results

Mean Intersection Error of Object Points

Table 2 presents the average and extreme values for different internal quality measures applied to the test results. The mean intersection errors after bundle adjustment obtained for the test datasets range between 7 m and 58 m and show only a minor variation (less than 10 percent) between different pre-processing types (all intersection errors refer to 3D errors at the 1σ level in this paper). The object point datasets were derived from the full tie point datasets subsequently used for DTM generation. Thus, the mean intersection errors are based on millions of point measurements. Points with intersection errors beyond a 95 percent confidence interval were considered as gross errors and discarded. Furthermore, points resulting from only two simultaneous stereo observations were discarded. The rejected points do not enter into the mean intersection error. Note that these restrictions still permit the provision of object points for a high percentage of the available tie points and thus lead to dense point sets suitable for DTM generation. We will address this point further in sub-sections to follow.

Besides the accuracy of image matching and of the geometric calibration of the sensor, the mean intersection error depends on the accuracy of the exterior orientation data, particularly the removal of systematic error components by bundle-adjustment. Based on adjusted orientation data, a good linear correlation between image resolution and point accuracy can be observed for the test dataset (Figure 5). According to linear regression, point accuracy is related to the ground resolution of the nadir image, i.e., the highest resolution of all panchromatic stereo images, by a factor of 0.9. Thus, on average, an accuracy of 0.9 pixels with respect to the best ground resolution is achieved for the object points. For the case of the standard regional mapping imaging mode with macro-pixel formats of 1×1 (nadir), 2×2, and 4×4, this translates to a point accuracy of 0.35 pixels with respect to the mean ground resolution of all five stereo channels. With few exceptions, all image sequences of the test dataset have been acquired applying this imaging mode, for which the ground resolution of the nadir channel is greater by a factor of about 2.6 than the mean stereo image resolution.

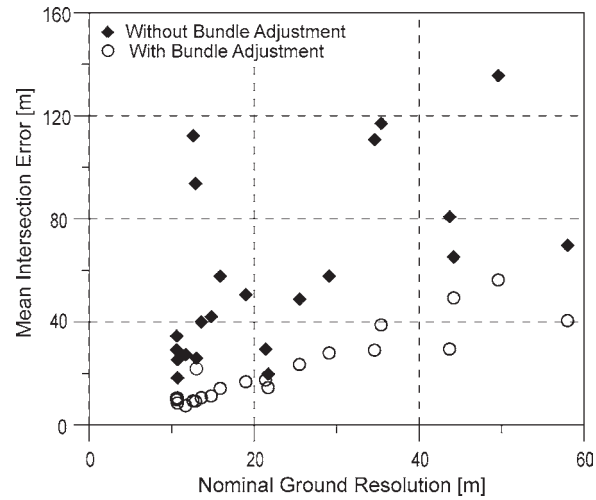

Figure 5. Mean intersection error of each dataset versus nominal ground resolution of the nadir channel. Filled squares: original exterior orientation data; open circles: adjusted exterior orientation data. Based on adaptive filtering of the stereo images.

For three orbits of the test dataset, a specific high-resolution stereo imaging mode has been applied, which enables the acquisition of full resolution imagery for three of the five panchromatic stereo channels, i.e., without macro-pixel binning. The remaining two panchromatic images are operated with macro-pixel format 2×2. In these cases, point accuracy reaches an even smaller fraction of the best ground resolution (60 to 80 percent). The highest mean intersection accuracy observed for the test dataset (7 m) has been achieved for one of these orbits.

It should be noted that the observed sub-pixel point accuracy also demonstrates the sub-pixel accuracy of the image matching process. Stereo image matching must necessarily provide an accuracy of a pixel fraction smaller than the above values because the error of the object points in addition reflects the uncertainty of the exterior and interior orientation data.

TABLE 2. RESULTS OF THE TEST RUNS FOR DIFFERENT PREPROCESSING TYPES. FIRST NUMBERS ARE AVERAGE VALUES FOR ALL DATASETS IN THE TEST. IN BRACKETS: RESPECTIVE MINIMUM AND MAXIMUM VALUES: (1) MEAN INTERSECTION ERROR FROM OVER-DETERMINED FORWARD INTERSECTION, BASED ON ORIENTATION DATA IMPROVED BY BUNDLE ADJUSTMENT, (2) MATCHING SUCCESS RATE: PERCENTAGE OF SUCCESSFULLY MATCHED IMAGE POINTS, (3) AND (4) PERCENTAGE OF TIE POINTS MATCHED IN ONLY THREE AND IN ALL FIVE STEREO IMAGES, RESPECTIVELY, AND (5) OBJECT POINT ACCEPTANCE: PERCENTAGE OF DERIVED OBJECT POINTS ACCEPTED FOR DTM GENERATION ACCORDING TO SELECTION CRITERIA

Quality measure Average Value (Min. / Max.)	**No Filtering**	**Invariant low pass**	**Adaptive low pass**
1) Mean Intersection Error [m]	21.0 (8.3 / 57.3)	23.0 (7.5 / 58.0)	20.5 (7.5 / 56.4)
2) Matching Success Rate [%]	49.0 (15.1 / 81.2)	63.3 (34.7 / 98.5)	66.1 (35.8 / 95.3)
3) Percentage of 3-fold intersections	15.5 (6.9 / 24.5)	38.3 (5.0 / 87.5)	14.4 (5.6 / 26.8)
4) Percentage of 5-fold intersections	61.8 (22.9 / 81.0)	39.6 (4.0 / 81.5)	62.8 (23.2 / 82.3)
5) Object Point Acceptance [%]	75.9 (62.5 / 85.0)	65.7 (33.4 / 92.4)	83.2 (63.4 / 94.5)

Figure 5 also shows that in the case of object points derived with initial data of exterior orientation, i.e., without bundle adjustment, no distinctive correlation between the mean intersection error and ground resolution can be observed. Given the fact that a good linear correlation is obtained from the same tie point dataset after bundle adjustment, we can relate the strong point accuracy variation observed before bundle adjustment to the variable accuracy of the initial data of exterior orientation. The actual improvement achieved through bundle adjustment changes considerably from orbit to orbit. The average, minimum and maximum mean point accuracy for the adaptive filtering case with bundle adjustment (20.5 m, 7.5 m, 56.4 m; Table 2) take values of 58.8 m, 18.3 m, and 135.6 m for initial orientation data, while the mean intersection errors of individual orbits are reduced through bundle adjustment by factors of between 1.2 and 11.9, with an average of 3.4.

Completeness of Image Matching and Object Point Density

When applying identical parameters and quality criteria for matching, both filtering types discussed above allow us to increase significantly the number of matched tie points (Table 2). The matching success rate (percentage of matched image points of the search grid) increases by 15 to 20 percent on average when compared to the case of original stereo images and never drops below the latter. For some datasets the number of matched points increases by a factor as large as 3. In some cases, a nearly complete coverage (>95 percent) of the entire search grid is possible. The search grids cover the full extent of the respective reference image (the nadir image), except for narrow borders on each side of the image that correspond to about half the width of the correlation window. Since high matching success rates could easily be a consequence of too permissive correlation thresholds, it is necessary to further evaluate the quality of the obtained tie points based on point accuracy and point density.

We use the term object point acceptance to denote the percentage of those tie points derived by matching which yield object points that can actually be used for DTM generation according to the selection criteria. Recall that, in the test runs, these criteria were an intersection error below the 95 percent level of the error distribution and a minimum number of three simultaneous observations. Table 2 and Figure 6 show that, after appropriate preprocessing, up to 95 percent of the matched tie points yielded acceptable object points under these selection criteria. The acceptance rate shows a strong variation between different test data sets. This is a direct consequence of differences in texture strength between the datasets and, as a consequence, different compression ratios. Secondly, the rates of point rejection were also found to vary strongly with the type of pre-processing. Adaptive filtering generally enables the highest number of accepted object points. While a quite constant increase of about 10 percent of the number of points is observed for the adaptive filtering case with respect to the "no filtering" case, invariant filtering leads to rather unsteady results. Both, few cases with point densities close to the two other preprocessing types as well as point rejections as large as 60 percent, leading to very sparse object point data sets, are observed in this case. The unsteady performance of space-invariant filtering again highlights the strong textural variability of the images. In the cases of high point rejection, the elimination of useful image texture by invariant filtering does lead to failure of image matching and blunders. Note that for the case of adaptive filtering, the width of the filter window is allowed to differ by a factor of up to 2.3 with respect to the invariant filtering case. The lower efficiency of multi-image matching in the case of invariant filtering is also evident from the average numbers of three-fold versus five-fold intersections (Table 2). Low percentages of multiple intersections (e.g., only 40 percent, five-fold intersections in the invariant filtering case) due to unsuccessful multi-image matching generally lead to a lower reliability of the object points. Conversely, after applying the adaptive filtering technique, 63 percent of the resulting object points can be based on five-fold intersections on average, and thus provide significantly higher reliability.

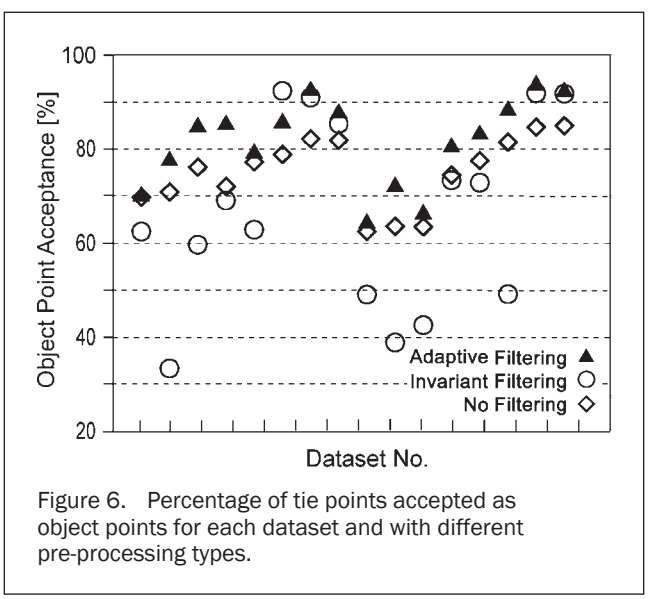

Figure 6. Percentage of tie points accepted as object points for each dataset and with different pre-processing types.

Lateral Variability of Object Point Density and Intersection Error

Coverage maps showing all grid cells of a DTM that contain at least one valid object point (Plates 1 and 2), i.e., the horizontal distribution of the object points, are of high significance, in addition to the rates of matching success and point acceptance, since image matching techniques tend to concentrate tie points in areas of strong image texture. Thus, in spite of high matching and acceptance rates, certain areas of the surface might still completely lack object point information. The grid values of the coverage maps show the respective height value or, alternatively, the mean local intersection error associated with the raster cell. The percentage of filled grid cells (or grid filling rate) is another measure of point density. Note that the filling rate depends on the choice of the grid spacing and thus has to be handled carefully when comparing DTMs with different grid size.

For the HRSC data based on adaptive filtering and with DTM grid spacing of 2 times the matching grid (or between 50 m and 225 m), an average filling rate of 59 percent is achieved. Using invariant filtering, the average filling rate reduces to 54 percent. The lowest filling rate (44 percent) is obtained when no image filtering is applied. In individual cases, filtering increases the filling rate by a factor of 1.6 (invariant) and 1.8 (adaptive), respectively.

The effect of image filtering on the filling rate of the DTM is shown for one example in Plate 1 (Hydrae Chasma, MEX orbit 1070), where coverage maps for the "no filtering" case and for the adaptive filtering case are compared. In addition to the improvement in coverage, some areas show smaller intersection errors after adaptive filtering. This is also reflected by a narrower distribution of intersection errors. Note that the majority of points are associated with intersection errors below 10 m in this example. A mean

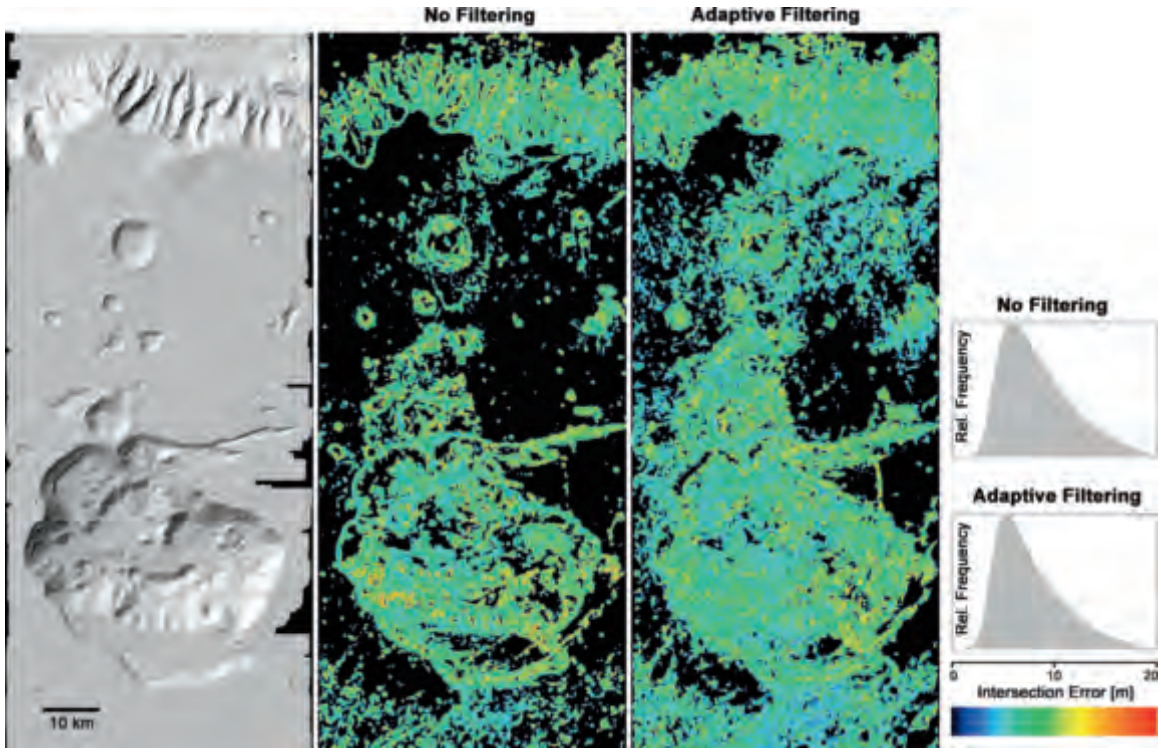

Plate 1. MEX orbit 1070, nominal nadir resolution 12 m/pixel, DTM grid 50 m. Left: shaded relief map from DTM based on adaptive filtering (see Plate 3b for corresponding nadir image); Middle: coverage map with color coded intersection error derived without image filtering (black: no object points); and Right: the same for adaptive filtering; associated relative frequency distributions of intersection error.

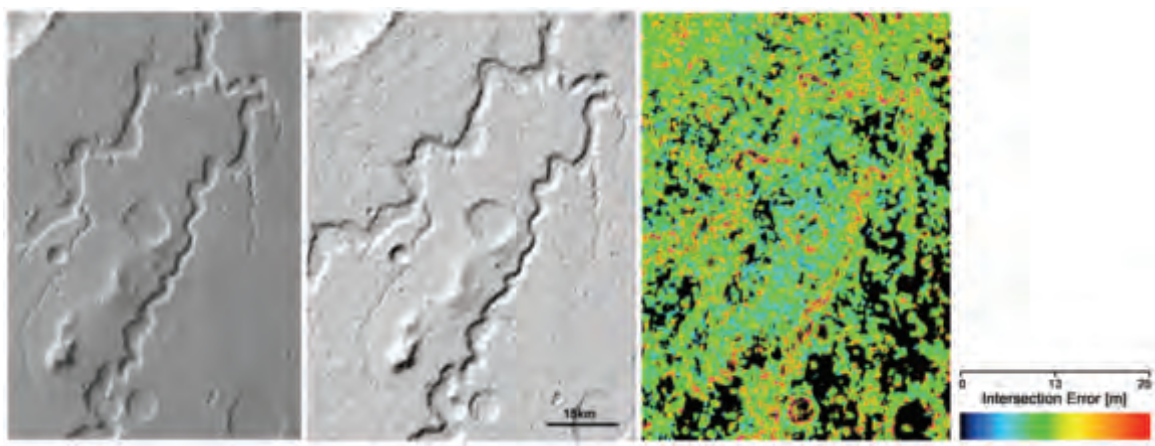

Plate 2. MEX orbit 905, nominal nadir resolution 15 m/pixel, DTM-grid 75 m. Left: orthoimage (nadir channel); Middle: shaded relief map from DTM based on adaptive filtering; and Right: coverage map with color coded intersection error (black: no object points).

intersection accuracy of 7 m is obtained for all accepted object points of this orbit.

A second example (Plate 2) is derived from MEX orbit 905 in the area of Nanedi Valles. In this example, as in the previous one, gaps in the DTM can clearly be identified with smooth and featureless plains in the nadir orthoimage. This implies that the matching procedure is successful on those areas with notable topography, while areas without tie points are smooth enough to permit closure of gaps by interpolation as long as the nearby edges of matched areas provide low measurement uncertainty, as demonstrated in Plates 1 and 2.

Deviation from MOLA Heights

While all quality measures addressed so far have been based on internal data, the MOLA DTM (NASA, 2003) represents valuable independent reference data for the external validation of the derived DTMs. The global topography provided by the Mars Orbiter Laser Altimeter (MOLA) experiment (Neumann *et al.*, 2003; Smith *et al.*, 2001; Abshire, 2000) has been recommended as reference model for Mars (Seidelmann *et al.*, 2002). MOLA profiles provide a vertical accuracy on the order of meters, depending on background signal and terrain roughness, and a horizontal uncertainty of <100 m (Neumann *et al.*, 2003). The height accuracy of individual MOLA point observations is thus expected to be equal or higher than the height accuracy of HRSC points. Conversely, the horizontal resolution of the MOLA DTM is lower than for HRSC since MOLA footprints have a diameter of about 170 m (Smith *et al.*, 2001), and a shot spacing of more than 300 m. The distance between individual measurement tracks is very small near the poles but amounts to several kilometers at the equator. For the gridded DTM product (463 m grid size), a horizontal accuracy of about 200 m and vertical accuracy on the order of 10 m can be assumed on average. For analyzing the deviation from MOLA heights, the HRSC DTMs (based on orientation data improved by bundle adjustment) are represented in the reference system adopted by the MOLA team (Smith *et al.*, 2001).

Table 3 reports different measures obtained for the deviation between HRSC and MOLA heights. In order to take into account the impact of interpolation at data gaps in both data sets, we consider also the deviations obtained when excluding HRSC data gaps as well as interpolated areas in between of the MOLA measurement tracks. The numbers indicate a close co-registration of the DTMs with mean height differences close to zero, for both the fully interpolated grids and the cases when height differences related to interpolated gaps are excluded. Averages close to zero are also observed across different sub-parts of DTMs, e.g., in difference maps (Plate 3). Conversely, the spread of the deviations decreases consistently when data gaps are excluded, as reflected by the averages of standard deviation and mean absolute value of difference and by the respective minimum and maximum values among the test datasets. When excluding all gap interpolation areas, standard deviations between 19.6 m and 73.4 m are observed for the test datasets, with an average of 41.0 m. As can be expected, differences associated with data gaps are thus responsible for a significant fraction of the total deviation between the fully interpolated DTMs.

The persisting deviation for the "no-gapsfill" case has to be attributed obviously to precision-related variances from both datasets, where the contribution of HRSC points can be estimated from the intersection errors (between 7.5 m and 56.4 m, dependent on image resolution, with an average of 20.5 m; see Table 2) and a height error of ~10 m can be assumed for MOLA. In addition, sampling effects associated with terrain curvature and related to the higher spatial resolution of HRSC might also cause a certain spread of the differences. Sampling effects are expected because height differences related to grid values are analyzed, while there are considerable differences in scale between the HRSC and MOLA DTMs (factors of about 2 to 9). Although we do not attempt to derive quantitative estimates for the contribution of sampling effects, the available numbers suggest that the two datasets conform well to each other within the uncertainty limits, considering that the HRSC intersection error together with an ~10 m MOLA height error already can account for the largest part of the total variance.

Further information on the nature of the height deviations between MOLA and HRSC can be gained from individual height profiles and the characteristics of difference maps (Figures 7 and 8, and Plate 3). The height deviation between fully interpolated DTMs but along MOLA tracks only is shown in the vertical sections of Figures 7 and 8 (lengths about 150 km) for a HRSC dataset with unusually low stereo image resolution (Figure 7: mean stereo resolution 102 m/pixel, nadir image 58 m/pixel, DTM grid 175 m) and for an example of a high-resolution HRSC data set (Figure 8: mean stereo resolution 17 m/pixel, nadir image 12 m/pixel, DTM grid 50 m). In both cases, a good overall correspondence in terms of mean difference is again observed. The residuals of the height components show standard deviations of 66 m for the low-resolution orbit and 30 m for the high-resolution orbit. Note that these profiles include interpolated data gaps in the HRSC DTM.

Profiles covering smooth terrain such as the profile from the high-resolution orbit shown in Figure 8b are particularly informative, because sampling effects should be very small on such areas. In this case, the standard deviation of the residuals reduces to 23 m, i.e., a value close to the minimum standard deviation observed for the entire test data set (19.6 m; Table 3). Figure 8b also shows the corresponding profile extracted from the HRSC DTM derived without filtering of the stereo imagery. In this case, mainly due to the occurrence of several notable local mismatches, the correlation with the MOLA profile is less close (standard deviation 45 m). Following the results previously described in the Results Section, we can relate these higher residuals to the smaller number of good quality object points that are achieved without image filtering. Note that smooth terrain with weak surface texture is among the most demanding surface types for stereo image matching. We can expect, therefore, maximum noise sensitivity for these areas, in agreement with the notable improvement achieved by image filtering.

Difference maps calculated from the fully interpolated HRSC and MOLA DTMs (Plate 3) generally show close agreement between both datasets in areas with dense point

TABLE 3. HEIGHT DIFFERENCE BETWEEN THE TEST DTM RESULTS (ADAPTIVE FILTERING CASE) AND THE MOLA 463 M-GRID DTM (NASA, 2003). FIRST NUMBERS ARE AVERAGE VALUES FOR ALL TEST DATASETS. IN BRACKETS: RESPECTIVE MINIMUM AND MAXIMUM VALUES AMONG THE DATASETS. FIRST LINE: DIFFERENCES BETWEEN THE FINAL GRID DTM PRODUCTS OF MOLA AND HRSC. SECOND LINE: DIFFERENCES ALONG MOLA MEASUREMENT TRACKS ONLY. THIRD LINE: DIFFERENCES ALONG MOLA MEASUREMENT TRACKS ONLY, AND EXCLUDING HRSC DATA GAPS (FILLED BY INTERPOLATION IN THE PREVIOUS CASES)

Measure of Deviation Average value (min/max)	**Offset**	**Standard Deviation of Difference**	**Mean Absolute Value of Difference**
Height Differences MOLA DTM versus HRSC DTM [m]	−3.0 (−7.9 / −0.3)	70.1 (39.1 / 107.4)	40.5 (22.4 / 68.8)
Height Differences MOLA Tracks versus HRSC DTM [m]	−3.1 (−9.3 / 0.4)	53.7 (19.9 / 98.0)	32.0 (13.7 / 62.9)
Height Differences MOLA Tracks versus HRSC DTM (no gaps fill) [m]	−2.7 (−8.0 / −0.2)	41.0 (19.6 / 73.4)	29.3 (13.8 / 53.9)

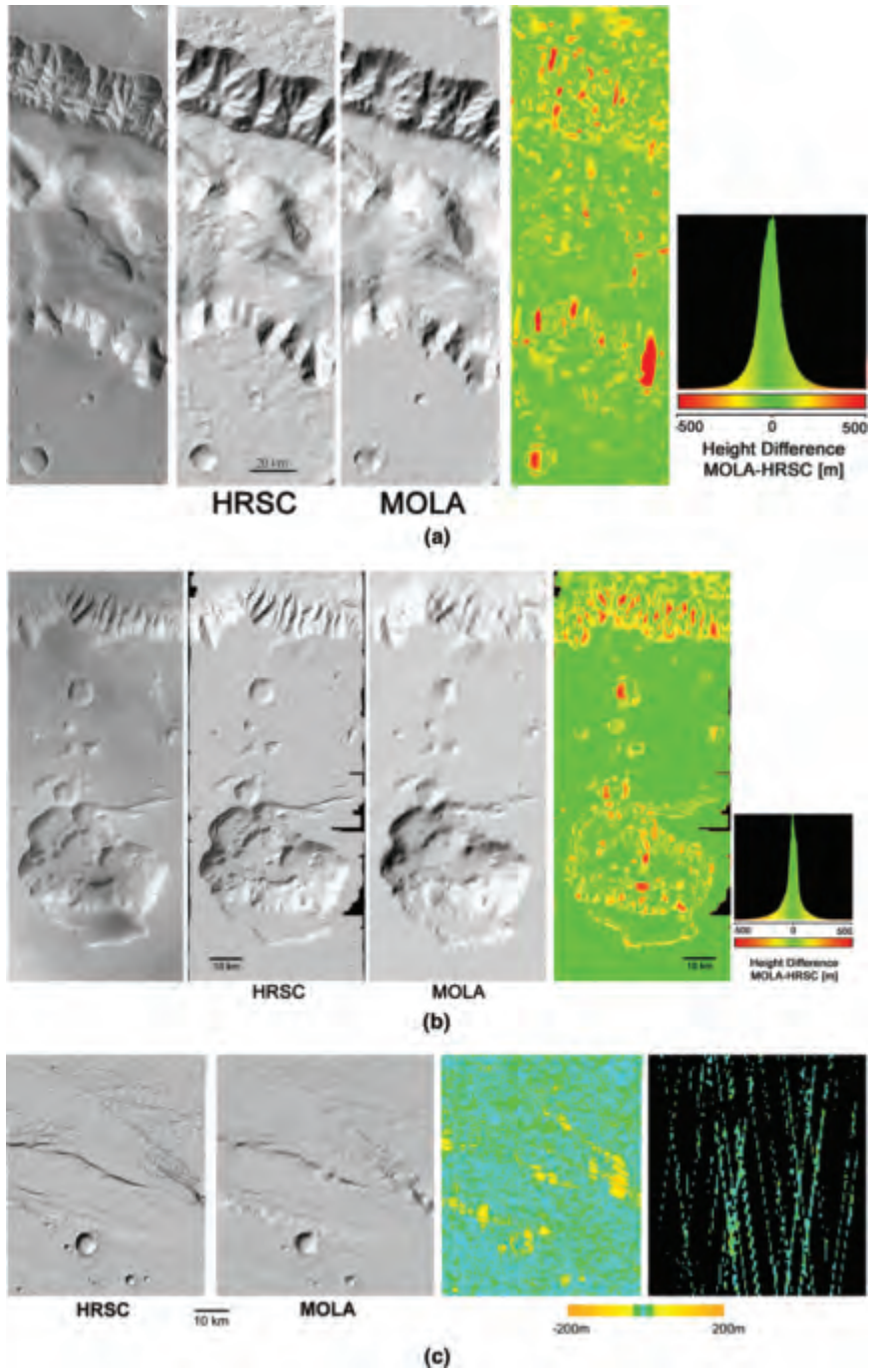

Plate 3. Comparison between MOLA and HRSC DTM, showing maximum differences associated with data gaps, and demonstrating the capability of HRSC DTM to represent complex and small surface forms: (a) and (b), Left: HRSC panchromatic orthoimages; shaded relief maps; Middle: difference maps for MOLA and HRSC; and Right: histograms of height differences. The color coding of the difference map is equal to the one of the histogram: (a) MEX orbit 515 (same example as in Figure 7), (b) MEX orbit 1070 (same example as in Plate 1 and Figure 8b), and (c) MEX orbit 2039. Left: shaded relief maps; Middle: difference map for fully interpolated MOLA and HRSC DTMs; and Right: difference map for MOLA and HRSC DTMs excluding data gaps filled by interpolation in both datasets. Note that color scale is modified in (c) for detailed representation of small deviations.

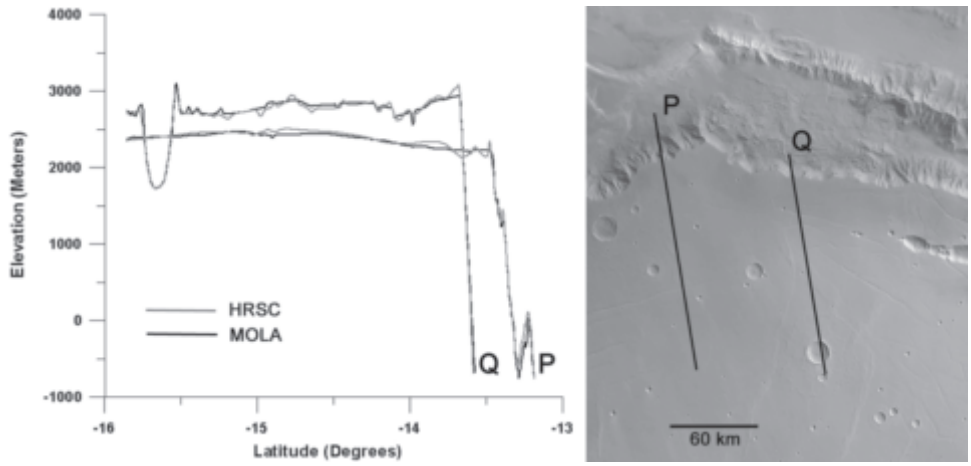

Figure 7. Two vertical sections along MOLA measurement tracks (MEX orbit 515). Grey: HRSC , Black: MOLA ; Right: panchromatic orthoimage with location of profiles.

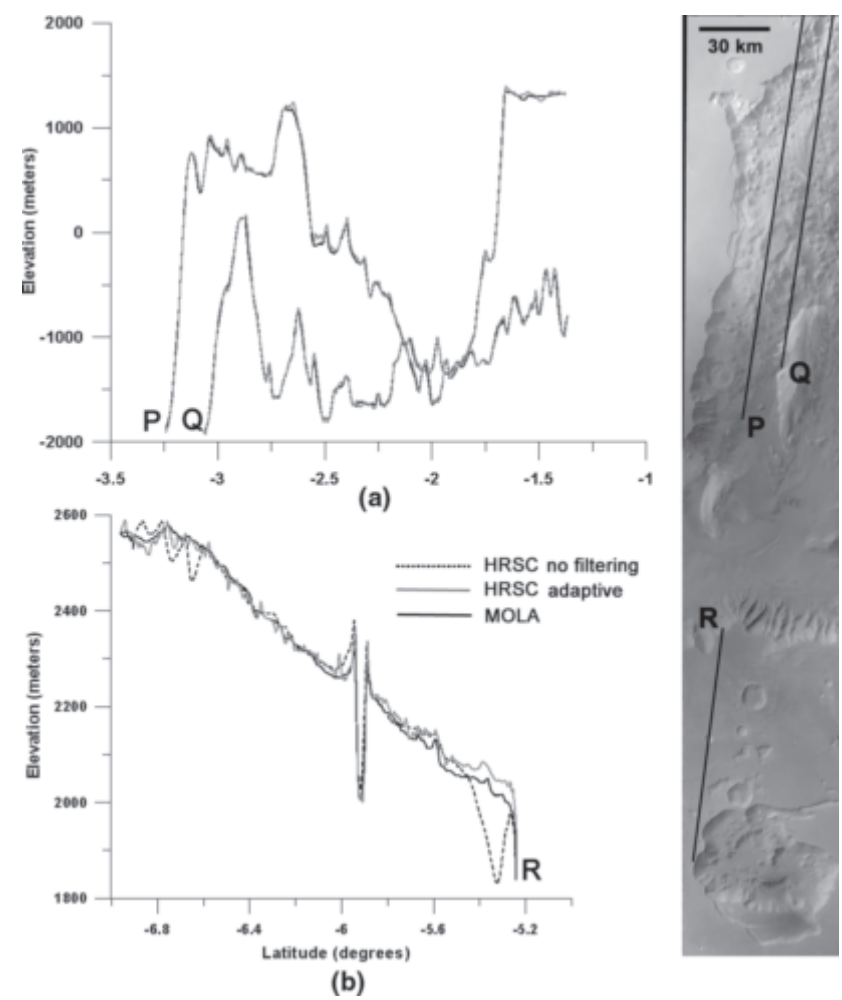

Figure 8. (a) Two vertical sections along MOLA measurement tracks (MEX orbit 1070). Grey: HRSC , Black: MOLA ; and (b) Vertical section on smooth topography for the same orbit. Grey: HRSC (adaptive image filtering), Dashed: HRSC (no image filtering), Black: MOLA . Right: panchromatic orthoimage with location of profiles.

coverage by the predominance of small differences on the order of up to few tens of meters (see also difference map excluding interpolation areas in Plate 3c). However, the deviation can be seen to amount to as much as few hundred meters for local areas associated with data gaps filled by interpolation, in particular, when the surface relief is strong. Accordingly, the standard deviations of the height differences on all grid cells for the examples shown in Plate 3 are 101 m (MEX orbit 515, low-resolution case, Plate 3a), 88 m (MEX orbit 1070, Plate 3b), and 68 m (MEX orbit 2039, Plate 3c).

The position and configuration of many of the larger interpolation-related deviations in the map view suggest that they are closely related to the local spacing and quality of individual MOLA measurement tracks (north-south elongated difference maxima in Plate 3; see also Heipke *et al.*, 2007). The larger height differences in these areas, typically representing high-relief terrain (e.g., slopes of deep depressions, calderas) and small relief elements (such as small craters and valleys), by comparison with the shaded relief maps and HRSC images, can most frequently be related to the higher capability of the HRSC DTMs to represent complex surface forms based on the higher spatial resolution and the exploitation of a laterally continuous coverage by object points. A more detailed representation of surface topography can also be observed for the low resolution HRSC dataset (Plate 3a), although less pronounced than for the datasets with higher ground resolution. For the HRSC DTM of MEX orbit 1070 (Plate 3b; Figure 9), the smallest craters clearly identifiable from the shaded relief map alone (and verified using the HRSC orthoimage) have a diameter of about 400 meters, i.e., smaller than the grid spacing of the MOLA DTM.

Summary and Conclusions - Implications for the Systematic Derivation of Mars Expr ess

HRSC High-resolution DTMs

In view of the systematic derivation of high-level data products from Mars Express HRSC data, we have studied the potential of the data for the generation of high-resolution DTMs of the surface of Mars. We have evaluated a number of internal and external quality measures for different processing variations, which were applied to a test dataset of 30 image sequences from orbits of the first mission year.

Based on exterior orientation data improved by bundle adjustment, we have demonstrated the feasibility of digital image matching at sub-pixel accuracy for HRSC images (better than 35 percent of the mean stereo resolution, on average). The improvement of the exterior orientation data by bundle adjustment leads to a significant reduction of the intersection error associated with the object points that are used for the generation of high-resolution DTMs (by a factor of about 3, on average). After adjustment, point accuracy shows a good linear correlation with the ground resolution of the images.

On average, only minor accuracy variation is observed for the derived 3D object points, when different preprocessing types are applied to reduce the effects of image compression on DTM generation. In this respect, previous findings on the feasibility of sub-pixel matching based on JPEG compressed stereo imagery (Parkes *et al.*, 1991) are confirmed. However, the most important difficulty for the matching of Mars Express HRSC imagery has been shown to consist in achieving a dense (in terms of spatial coverage) and reliable matching result (i.e., high percentage of multiple intersections, elimination of false correlations). In this respect, filtering of the stereo imagery by a signal adaptive technique before image matching clearly improves the results when compared to the cases of space-invariant image filtering and of matching the original stereo images. In particular, adaptive filtering allows for the highest matching success rates and the highest acceptance of corresponding object points. It has been shown that the filling rates of the final DTM products can nearly be doubled by adaptive filtering. Conversely, space-*invariant* filtering has been shown to yield object points of strongly variable and sometimes poor quality, resulting in low filling rates of the DTM grid due to high rates of point rejection. It can therefore be concluded that a constant filtering bandwidth does not properly account for the high variability of textural properties and compression features of HRSC imagery. Still lower filling rates are, however, obtained when no image filtering is applied, because significantly lower matching success rates are achieved. In summary, adaptive filtering turned out to be the most reliable option and is considered as an essential requirement for the systematic generation of HRSC high-resolution DTMs.

From the test results based on adaptive image filtering, the most important quality-related figures that can be expected for HRSC high-resolution DTMs can be summarized as follows. Matching of HRSC imagery at a resolution suitable for the derivation of high-resolution DTMs (up to 50 m grid spacing) is feasible at an average success rate of 66 percent, i.e., two of three pixels of the search grid are successfully matched on average. In some cases a nearly complete coverage (95 percent) of the search grid with tie points is possible. On average, 90 percent of these successfully matched points can be matched in at least three stereo images, providing a high robustness against erroneous point determinations. For the most common operation mode of the camera, the expected 3D accuracy of the derived object points is 35 percent of the mean stereo image resolution (or 90 percent of the best ground resolution). A specific high-resolution stereo imaging mode allows for even higher mean intersection accuracy of about 70 percent of the best ground resolution. The highest mean intersection accuracy observed for the test dataset has been achieved for one of the orbits in which this mode was operated.

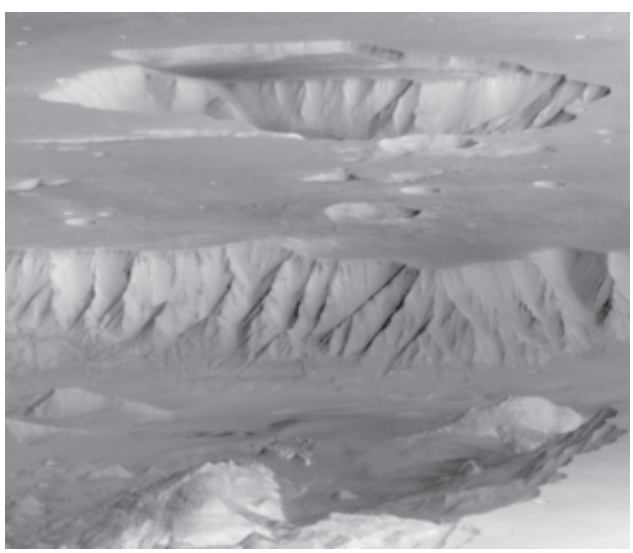

Figure 9. MEX orbit 1070, perspective view of example in Plate 3b derived from DTM and orthoimage. Viewing direction is from North to South.

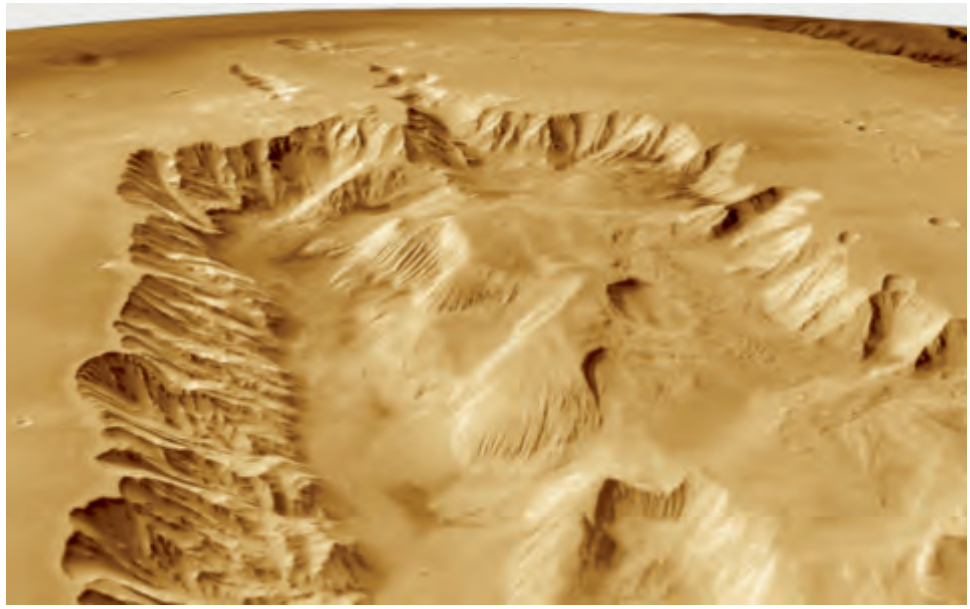

Plate 4. Perspective view of eastern Candor Chasma (Valles Marineris) generated from a mosaic of HRSC DTM s and orthoimages of different orbits.

Considering the distribution of ground resolutions within the entire HRSC dataset (and depending on the further development of the mission), it can be expected that high-resolution DTMs with a spatial resolution of 50 to75 m and a 3D point accuracy of about 10 m can be derived for large parts of the surface of Mars. These data products allow for 3D analysis and visualization at scales close to the ground resolution of the imagery (Figure 9; Plate 4).

Analyzing height differences with respect to the MOLA DTM also provides useful information on the quality of HRSC DTMs. While average height differences close to zero confirm the successful registration of the HRSC DTMs to the global MOLA reference system, considerable height differences between the two DTM datasets in terms of mean absolute value and standard deviation are also observed. These can be attributed mainly to data gaps and the precision of point measurements on both sides. Comparison of shaded relief maps and height difference maps also show differences in resolved detail that are related to the area-based approach and the higher spatial resolution of HRSC. In particular, HRSC DTMs can provide a more detailed representation of complex terrain with strong relief or small morphologic elements, which together with other factors such as the use of MOLA data as a planetary reference system, underlines the complementarity of the two approaches.

Acknowledgments

We gratefully acknowledge the support of the participants of the HRSC experiment team of DLR, in particular of Thomas Roatsch, Klaus-Dieter Matz, and Marita Wählisch, and of the Mars Express Project teams at ESTEC and ESOC. We also thank for thoughtful comments by the three anonymous reviewers and by members of the HRSC Co-Investigator Team, in particular by David A. Williams, Jan-Peter Muller, Gottfried Schwarz, and Ernst Hauber.

References

Abshire, J.B., 2000. Mars Orbiter Laser Altimeter: Receiver model and performance analysis, *Applied Optics*, 39(15):2449–2460.

Ackermann, F., 1984. High precision digital image correlation, *Proceedings of the 39th Photogrammetric Week*, Schriftenreihe der Universität Stuttgart, 9:231–243.

Albertz, J., M. Attwenger, J. Barrett, S. Casley, P. Dorninger, E. Dorrer, H. Ebner, S. Gehrke, B. Giese, K. Gwinner, C. Heipke, E. Howington-Kraus, R.L. Kirk, H. Lehmann, H. Mayer, J.-P. Muller, J. Oberst, A. Ostrovskiy, J. Renter, S. Reznik, R. Schmidt, F. Scholten, M. Spiegel, M. Wählisch, G. Neukum, and the HRSC Co-Investigator Team, 2005. HRSC on Mars Express – Photogrammetric and cartographic research, *Photogrammetric Engineering & Remote Sensing*, 71(10):1153–1166.

Astrium, 2001. *Mars Express - System Requirements Specification*, Technical Report MEX.MMT.TN.0519, EADS Astrium GmbH.

Ebner, H., T. Ohlhof, and E. Putz, 1996. Orientation of MOMS-02/D2 and MOMS-2P imagery, *International Archives of Photogrammetry and Remote Sensing*, 31(B3):158–164.

Ebner H., M. Spiegel, B. Albert, G. Bernd, G. Neukum, and the HRSC Co-Investigator Team, 2004. Improving the exterior orientation of Mars Express HRSC imagery, *International Archives of Photogrammetry and Remote Sensing*, 34(B4):852–858.

Grün, A., and L. Zhang, 2003. Sensor modelling for aerial triangulation with Three-Line-Scanner (TLS) Imagery, *Photogrammetrie, Fernerkundung, Geoinformation*, 2:85–98.

Gwinner, K., E. Hauber, R. Jaumann, and G. Neukum, 2000. High-resolution, digital photogrammetric mapping: A tool for Earth science, *EOS Transactions*, American Geophysical Union, 81(44):513–520.

Gwinner, K., E. Hauber, H. Hoffmann, F. Scholten, R. Jaumann, G. Neukum, M. Coltelli, and G. Puglisi, 1999. The HRSC-A experiment on high resolution imaging and DEM generation at the Aeolian Islands, *Proceedings of the 13th International Conference on Applied Geologic Remote Sensing*, 01–03 March, Vancouver, Canada, ERIM International, Ann Arbor, Michigan, Vol. I, pp. 560–569.

Hechler, M., and A. Yanez, 2000. *Mars Express - Consolidated Report on Mission Analysis Issue 2.0*, Technical Report MEXESC-RP-5500, European Space Agency.

Heipke C., R. Schmidt, R. Brand, J. Oberst, G. Neukum, and the HRSC Co-investigator Team, 2004. Performance of automatic tie point extraction using HRSC imagery of the Mars Express Mission, *International Archives of Photogrammetry and Remote Sensing*, 34(B4):846–851.

Heipke C., J. Oberst, J. Albertz, M. Attwenger, P. Dorninger, E. Dorrer, M. Ewe, S. Gehrke, K. Gwinner, H. Hirschmüller, J.R. Kim, R.L. Kirk, H. Mayer, J.-P. Muller, R. Rengarajan, M. Rentsch, R. Schmidt, F. Scholten, J. Shan, M. Spiegel, M. Wählisch, G. Neukum, 2007. Evaluating planetary digital terrain models - The HRSC DTM test, *Planetary and Space Science*, 55:2173–2191.

Jaumann R., G. Neukum, T. Behnke, T.C. Duxbury, K. Eichentopf, J. Flohrer, S. van Gasselt, B. Giese, K. Gwinner, E. Hauber, H. Hoffmann, A. Hoffmeister, U. Köhler, K.-D. Matz, T.B. McCord, V. Mertens, J. Oberst, R. Pischel, D. Reiss, E. Ress, T. Roatsch, P. Saiger, F. Scholten, G. Schwarz, K. Stephan, M. Wählisch, and the HRSC Co-Investigation Team, 2007. The High-Resolution Stereo Camera (HRSC) experiment on Mars Express: instrument aspects and experiment conduct from interplanetary cruise through the nominal mission, *Planetary and Space Science*, 55:928–952.

JPL, 2003. The VICAR Image Processing System, URL: *http://www.mipl.jpl.nasa.gov/external/vicar.html*, Jet Propulsion Laboratory, Multimission Image Processing Laboratory (MIPL) (last date accessed: 17 June 2009).

Kirk, R.L., E. Howington-Kraus, B. Redding, D. Galuszka, T.M. Hare, B.A. Archinal, L.A. Soderblom, and J.M. Barrett, 2003. High-resolution topomapping of candidate MER landing sites with Mars Orbiter Camera narrow-angle images, *Journal of Geophysical Research*, 108 (E12), 8088, doi:10.1029/2003JE002131.

Kirk, R.L., E. Howington-Kraus, D. Galuszka, B. Redding and T.M. Hare, 2006. Topomapping of Mars with HRSC images, ISIS, and a commercial stereo workstation, *International Archives of Photogrammetry, Remote Sensing*, 36(4A):293–298.

Kirk, R.L., E. Howington-Kraus, M.R. Rosiek, D. Cook, J. Anderson, K. Becker, B.A. Archinal, L. Keszthelyi, R. King, A.S. McEwen, and the HiRISE Team, 2007. Ultrahigh resolution topographic mapping of Mars with HiRISE stereo images: methods and first results, *Proceedings of the 38th Lunar and Planetary Science Conference*, 12–16 March, Houston, Texas (Lunar and Planetary Institute), Abstract No. 1428.

Kuo, C.J., and R.J. Hsieh, 1995. Adaptive postprocessor for block-encoded images, *IEEE Transactions on Circuits and Systems for Video Technology*, 5:298–304.

Malin, M.C, and K.S. Edgett, 2001. Mars Global Surveyor Mars Orbiter Camera: Interplanetary cruise through primary mission, *Journal of Geophysical Research*, 106(E10):23429–23570.

McEwen, A., E. Eliason, J. Bergstrom, N. Bridges, C. Hansen, W. Delamere, J. Grant, V. Gulick, K. Herkenhoff, L. Keszthelyi, R. Kirk, M. Mellon, S. Squyres, N. Thomas, and C. Weitz, 2007. Mars Reconnaissance Orbiters's High Resolution Imaging Science Experiment (HiRISE), *Journal of Geophysical Research*, 112: E05S02, doi:10.1029/2005JE002605.

Müller, F., 1991. *Photogrammetrische Punktbestimmung mit Bilddaten Digitaler Dreizeilenkameras*. Deutsche Geodätische Kommission, Series C, No. 327, Munich, 82 p.

NASA, 2003. Mars Global Surveyor Laser Altimeter Mission Experiment Gridded Data Record MGS-M-MOLA-5-MEGDR-L3-V1.0, URL: *http://pds.jpl.nasa.gov*, National Aeronautics and Space Administration Planetary Data System (last date accessed: 17 June 2009).

Neukum, G., R. Jaumann, and the HRSC Co-Investigator Team, 2004. *HRSC: The High Resolution Stereo Camera of Mars Express*, ESA Special Publications, SP-1240.

Neumann, G.A., F.G. Lemoine, D.E. Smith, and M.T. Zuber, 2003. The Mars Orbiter Laser Altimeter archive: Final precision experiment data record release and status of radiometry, *Proceedings of the 34th Lunar and Planetary Science Conference*, 17–21 March, Houston, Texas (Lunar and Planetary Institute), Abstract No. 1778.

Nosratinia, A., 2001. Enhancement of JPEG-compressed images by re-application of JPEG, *Journal of VLSI Signal Processing*, 27(2):69–79.

Nozette S., P. Rustan, L.P. Pleasance, J.F. Kordas, I.T. Lewis, H.S. Park, R.E. Priest, D.M. Horan, P. Regeon, C.L. Lichtenberg, E.M. Shoemaker, E.M. Eliason, A.S. McEwen, M.S. Robinson, P.D. Spudis, C.H. Acton, B.J. Buratti, T.C. Duxbury, D.N. Baker, B.M. Jakosky, J.E. Blamont, M.P. Corson, J.H. Resnick, C.J. Rollins, M.E. Davies, P.G. Lucey, E. Malaret, M.A. Massie, C.M. Pieters, R.A. Reisse, R.A. Simpson, D.E. Smith, T.C. Sorenson, R.W. Vorder Breugge, and M.T. Zuber, 1994. The Clementine Mission to the Moon: scientific overview, *Science*, 266:1835–1839.

O'Rourke, T.P., and R.L. Stevenson, 1995. Improved image decompression for reduced transform coding artifacts, *IEEE Transactions on Circuits and Systems for Video Technology*, 5:490–499.

Parkes, S.M., M.J.A. Zemerly, and J.-P. Muller, 1991. Image data compression and its effects on stereo height extraction processing, *Proceedings of IGARSS '91*, Helsinki (Geoscience and Remote Sensing Society), pp. 1449–1452.

Reeves, H.C., and J.S. Lim, 1984. Reduction of blocking artifacts in image coding, *Optical Engineering*, 23:34–37.

Robinson, C., B. Montgomery, and C. Fraser, 1995. The effects of image compression on automated DTM generation, *Proceedings of Photogrammetric Week '95* (D. Fritsch and D. Hobbie, editors), Heidelberg, pp. 255–262.

Sandau, R., B. Braunecker, H. Driescher, A. Eckardt, S. Hilbert, J. Hutton, W. Kirchhofer, E. Lithopoulos, R. Reulke, and S. Wicki, 2000. Design principles of the LH Systems ADS40 Airborne Digital Sensor, *International Archives of Photogrammetry and Remote Sensing*, 33(B1):258–265.

Schmidt, R., M. Spiegel, C. Heipke, J. Oberst, G. Neukum, and the HRSC Co- Investigator Team, 2005. Automatic tie point generation for the processing of HRSC imagery of the Mars Express Mission, *Proceedings of the 36th Lunar and Planetary Science Conference*, 14–18 March, Houston, Texas (Lunar and Planetary Institute), Abstract No. 1769.

Scholten, F., and K. Gwinner, 2004. Operational parallel processing in digital photogrammetry - strategy and results using different multi-line cameras, *International Archives of Photogrammetry and Remote Sensing*, 34(B2):408–413.

Scholten, F., K. Gwinner, T. Roatsch, K.-D. Matz, M. Wählisch, B. Giese, J. Oberst, R. Jaumann, G. Neukum, and the HRSC Co-Investigator Team, 2005. Mars Express HRSC Data Processing - Methods and operational aspects, *Photogrammetric Engineering & Remote Sensing*: 71(10):1143–1152.

Schwarz, G., 1995. *On-Board Image Data Compression – The Data Compression Electronics of the High Resolution Stereo Camera (HRSC)*, Technical Report, German Aerospace Center (DLR), German Remote Sensing Data Center, Wessling, Germany.

Seidelmann, P.K., V.K. Abalakin, M. Bursa, M.E. Davies, C. de Bergh, J.H. Lieske, J. Oberst, J.L. Simon, E.M. Standish, P. Stooke and P.C. Thomas, 2002. Report of the IAU/IAG Working Group on Cartographic Coordinates and Rotational Elements of the Planets and Satellites: 2000, *Celestial Mechanics and Dynamical Astronomy*, 82(1):83–111.

Smith, D.E., M.T. Zuber, H.V. Frey, J.B. Garvin, and J.W. Head, 2001. Mars Orbiter Laser Altimeter (MOLA): Experiment summary after the first year of global mapping of Mars, *Journal of Geophysical Research*, 106(E10):23689–23722.

Snyder, C.W., 1979. The extended mission of Viking, *Journal of Geophysical Research*, 84:7917–7933.

Spiegel, M., R. Schmidt, U. Stilla, G. Neukum, and the HRSC Co-Investigator Team, 2005. Adapting HRSC imagery of Mars Express Mission to Mars Observer Laser Altimeter Data, *Proceedings of the 36th Lunar and Planetary Science Conference*, 14–18 March, Houston, Texas (Lunar and Planetary Institute), Abstract No. 1761.

Spiegel, M., 2007. Improvement of interior and exterior orientation of the three line camera HRSC with a simultaneous adjustment, *International Archives of Photogrammetry and Remote Sensing*, 36 (3/W49B):161–166.

Wu, S., and F. Doyle, 1990: *Topographic Mapping, Planetary Mapping* (R. Greeley and R.M. Batson, editors), Cambridge University Press, Cambridge, N.Y., pp. 169–207.

Wewel, F., F. Scholten, and K. Gwinner, 2000. High Resolution Stereo Camera (HRSC) - Multispectral 3D-data acquisition and photogrammetric data processing, *Canadian Journal of Remote Sensing*, 26(5):466–474.

Yang, Y, N. Galatsanos, and A. Katsaggelos, 1993. Regularized reconstruction to reduce blocking artifacts of block discrete cosine transform compressed images, *IEEE Transactions on Circuits and Systems for Video Technology*, 3:421–432.

Yoon, J.S. and J. Shan, 2005. Combined adjustment of MOC stereo imagery and MOLA altimetry data, *Photogrammetric Engineering & Remote Sensing*, 71(10):1179–1186.

(Received 01 May 2008; accepted 01 July 2008; revised 02 January 2009)